Massive formation of early diagenetic dolomite in the Ediacaran ocean: Constraints on the "dolomite problem"

Biao Chang[a,b], Chao Li[a,1], Deng Liu[a], Ian Foster[c], Aradhna Tripati[c,d,e], Max K. Lloyd[f], Ingrid Maradiaga[d,e], Genming Luo[a], Zhihui An[g], Zhenbing She[a], Shucheng Xie[a], Jinnan Tong[a], Junhua Huang[b,1], Thomas J. Algeo[a,b,h], Timothy W. Lyons[i], and Adrian Immenhauser[j]

[a]State Key Laboratory of Biogeology and Environmental Geology, China University of Geosciences, Wuhan 430074, China; [b]State Key Laboratory of Geological Processes and Mineral Resources, China University of Geosciences, Wuhan 430074, China; [c]UMR6538 Géosciences Océan, Institut Universitaire Européen de la Mer, 29280 Plouzané, France; [d]Department of Earth, Planetary, and Space Sciences, University of California, Los Angeles, CA 90095; [e]Department of Atmospheric and Oceanic Sciences, Institute of the Environment and Sustainability, University of California, Los Angeles, CA 90095; [f]Division of Geological and Planetary Sciences, California Institute of Technology, Pasadena, CA 91125; [g]Hubei Key Laboratory of Paleontology and Geological Environment Evolution, Wuhan Institute of Geology and Mineral Resources, Wuhan 430205, China; [h]Department of Geology, University of Cincinnati, Cincinnati, OH 45221-0013; [i]Department of Earth and Planetary Sciences, University of California, Riverside, CA 92521; and [j]Institute for Geology, Mineralogy, and Geophysics, Ruhr University Bochum, D-44801 Bochum, Germany

Paleozoic and Precambrian sedimentary successions frequently contain massive dolomicrite [$CaMg(CO_3)_2$] units despite kinetic inhibitions to nucleation and precipitation of dolomite at Earth surface temperatures (<60 °C). This paradoxical observation is known as the "dolomite problem." Accordingly, the genesis of these dolostones is usually attributed to burial–hydrothermal dolomitization of primary limestones ($CaCO_3$) at temperatures of >100 °C, thus raising doubt about the validity of these deposits as archives of Earth surface environments. We present a high-resolution, >63-My-long clumped-isotope temperature ($T_{\Delta 47}$) record of shallow-marine dolomicrites from two drillcores of the Ediacaran (635 to 541 Ma) Doushantuo Formation in South China. Our $T_{\Delta 47}$ record indicates that a majority (87%) of these dolostones formed at temperatures of <100 °C. When considering the regional thermal history, modeling of the influence of solid-state reordering on our $T_{\Delta 47}$ record further suggests that most of the studied dolostones formed at temperatures of <60 °C, providing direct evidence of a low-temperature origin of these dolostones. Furthermore, calculated $\delta^{18}O$ values of diagenetic fluids, rare earth element plus yttrium compositions, and petrographic observations of these dolostones are consistent with an early diagenetic origin in a rock-buffered environment. We thus propose that a precursor precipitate from seawater was subsequently dolomitized during early diagenesis in a near-surface setting to produce the large volume of dolostones in the Doushantuo Formation. Our findings suggest that the preponderance of dolomite in Paleozoic and Precambrian deposits likely reflects oceanic conditions specific to those eras and that dolostones can be faithful recorders of environmental conditions in the early oceans.

Doushantuo Formation | clumped isotope | early diagenesis | carbonate geochemistry | early oceans

Paleozoic and Precambrian sedimentary successions often include massive dolostone bodies that are hundreds of meters in thickness and hundreds of kilometers in lateral extent (1, 2). In contrast, comparably massive dolomite successions are rare in younger marine successions (2), although modern seawater is oversaturated with respect to dolomite by one to two orders of magnitude (1). Laboratory experiments have demonstrated that the difficulty of dolomite synthesis under Earth surface conditions (3) is likely due to hydration effects that hinder incorporation of Mg^{2+} into the dolomite crystal lattice (4). Given the kinetic barriers that inhibit low-temperature dolomite nucleation and precipitation, the existence of massive Paleozoic and Precambrian dolomite deposits has puzzled geologists for more than two centuries (5, 6), giving rise to the so-called "dolomite problem."

To resolve the dolomite problem, massive dolostones are usually attributed to slow burial or hydrothermal dolomitization of calcite or aragonite precursors by Mg-rich fluids at temperatures of >100 °C [i.e., the burial–hydrothermal dolomitization model; $2CaCO_3 + Mg^{2+} \rightarrow CaMg(CO_3)_2 + Ca^{2+}$ or $CaCO_3 + Mg^{2+} + CO_3^{2-} \rightarrow CaMg(CO_3)_2$] (5). This model is supported by many petrographic observations (e.g., coarse dolomite cements, saddle dolomites) and geochemical evidence (e.g., elemental and isotopic compositions) from both Phanerozoic (7) and Proterozoic dolostones (8). Importantly, dolostones formed in the burial domain likely record the properties of formation fluids at depth rather than those of syndepositional marine waters. In such a case, dolomite-hosted geochemical data [e.g., carbonate $\delta^{13}C$ ($\delta^{13}C_{carb}$), which is widely used in analysis of global and local marine carbon cycling] would be of little use in reconstruction of surface environmental conditions and processes in deep-time systems.

Significance

Massive Paleozoic and Precambrian dolostone successions have long puzzled geologists in light of the kinetic barriers that inhibit low-temperature dolomite nucleation and precipitation (i.e., the "dolomite problem"). Significantly, the widely accepted hypothesis that such massive dolomites are the product of burial–hydrothermal dolomitization challenges their validity as archives of Earth surface environments. Here, we place constraints on the formation of massive dolomicrite deposits of the Ediacaran Doushantuo Formation (South China), demonstrating their syndepositional (i.e., early diagenetic) formation over a >63-My interval. Our findings suggest that the "dolomite problem" may be a product of specific conditions common if not persistent in Paleozoic and Precambrian oceans, and that massive dolostone successions may be faithful recorders of environmental conditions in the early oceans.

EARTH, ATMOSPHERIC, AND PLANETARY SCIENCES

In contrast, other studies have asserted that dolomites can form at low temperatures in marine porewaters during early diagenesis (as reviewed in ref. 5). Major early diagenetic mechanisms invoking seawater as the dolomitizing fluid include the sabkha model, which hypothesizes early diagenetic dolomitization of calcite or aragonite precursors at temperatures of <60 °C in evaporative settings (such as hypersaline ponds associated with sabkhas) via reflux of Mg-rich seawaters (1, 9). Another proposed mechanism is the organogenic dolomite model, which involves direct precipitation of very high-Mg calcite and non-stoichiometric or stoichiometric dolomite $[Ca^{2+} + Mg^{2+} + 2CO_3^{2-} \rightarrow CaMg(CO_3)_2]$ from seawater or near-surface porewaters through microbial-organic mediation (10, 11), followed by transformation to ordered dolomite following Ostwald's rule (12) during early marine burial (13–15). The sabkha model, supported by remnants of evaporitic minerals, has been invoked for the Triassic Dolomia Principale of the Dolomite Mountains of Italy and other shallow-marine dolostone units (16). The organogenic dolomite model is supported by both laboratory culture experiments and some modern field observations (10, 11, 13–15). These early diagenetic models are undoubtedly relevant to understanding massive dolostone formation in deep time (e.g., ref. 17); however, only minor amounts of dolomite are formed in modern surface environments, and these are usually embedded in calcitic and aragonitic host sediments (see review in ref. 5). Therefore, any direct evidence for massive formation of early diagenetic dolomites in deep time likely elevates the past importance of early formation pathways.

Here, we present a >63-My-long carbonate clumped-isotope (Δ_{47}) paleotemperature ($T_{\Delta 47}$) record for dolostones of the Ediacaran Doushantuo Formation in South China. The $T_{\Delta 47}$ technique can quantitatively constrain the formation temperature of a dolomite sample without a priori knowledge of original paleoseawater $\delta^{18}O$ values (18) (*Methods*). Our $T_{\Delta 47}$ record, in combination with coexisting elemental, isotopic, and petrographic data, provides insight into the mechanisms of massive dolostone formation in deep time.

Geological Setting and Sampling

The Doushantuo Formation of the Yangtze Platform (South China) is a succession of marine carbonate (mainly dolomite), siliciclastic, and phosphatic sedimentary rocks deposited immediately after the global-scale Neoproterozoic Marinoan (or Nantuo in South China) glaciation at paleolatitudes of ~30 °N (19) (Fig. 1 and *SI Appendix*, Fig. S1A). The Doushantuo Formation shows increasing carbonate content with decreasing water depth from the southeast (basinal) to the northwest (shallow marine) regions of the Yangtze Platform, with carbonate-dominated deposition over 1.5×10^5 km^2 (*SI Appendix*, Fig. S1B). Zircon U–Pb ages indicate that the Doushantuo Formation was deposited from ~635 to 551 Ma (20), with carbonate deposition occurring mainly during the ~614- to 551-Ma interval (20, 21).

The samples of the present study were collected from the Doushantuo Formation in two drillcores (ZK312-P312 and ZK407) from the Zhangcunping area (Hubei Province) and represent shallow-marine platform carbonates (*SI Appendix*, Fig. S1 B and C). The ZK312-P312 drillcore was collected in Duanjiang Village (31°28′ 25.73″N, 111°11′36.62″E), Baokang County, and the ZK407 drillcore was collected ~12 km further to the southeast (*SI Appendix*, Fig. S1C). In ZK312-P312, the Doushantuo Formation overlies Cryogenian glacial diamictites of the Nantuo Formation and has a total thickness of ~138 m. It is subdivided into four lithostratigraphic units (Members I–IV; Fig. 1 and *SI Appendix*, Fig. S2) (22). The 2.9-m-thick Member I consists of thick-bedded, light gray microcrystalline dolostone with stromatactis-like cavities. The 75-m-thick Member II consists of 13 m of phosphatic black shales, 14.5 m of thick-bedded gray microcrystalline dolostones, 21.3 m of thin-bedded gray microcrystalline dolostone containing phosphorite layers, and

26.2 m of thin-bedded dark gray microcrystalline dolostone containing large chert nodules. The 46.9-m-thick Member III consists of thin- to medium-bedded gray microcrystalline dolostone intercalated with black shales and chert layers in its middle and upper portions, respectively. The 12.9-m-thick Member IV consists of thin-bedded dark gray microcrystalline dolostone that contrasts with the overlying thick-bedded light gray dolostone of the lower Dengying Formation. In ZK407, the Doushantuo Formation has a total thickness of ~94.5 m and exhibits the same lithological subdivisions as in the ZK312-P312 drillcore, although with different thicknesses: 2.8 m for Member I, 50.4 m for Member II, 27.4 m for Member III, and 13.9 m for Member IV (*SI Appendix*, Fig. S2).

Our samples span the entire >63-My-long interval of dolomite units within the Doushantuo Formation (i.e., Members I–IV except for the black shale interval in Member II), which is represented by ~125 m in the ZK312-P312 core and ~93 m in the ZK407 core (Fig. 1 and *SI Appendix*, Fig. S2). Because of their near-identical lithostratigraphic successions, the two drillcores can be accurately correlated. The two study cores can also be correlated to the intrashelf-basin Jiulongwan section in the Yangtze Gorges area and to other sections of the Doushantuo Formation and its lateral equivalents across the Yangtze Platform based on available litho-, bio-, and chemostratigraphic data (*SI Appendix*, Fig. S2 and ref. 22). This high-resolution correlation framework allows us to integrate the $T_{\Delta 47}$ and other proxy records in the drillcores (*SI Appendix*, Fig. S2) and then extrapolate them for a regional perspective.

Results and Discussion

$T_{\Delta 47}$ Records. The ZK312-P312 and ZK407 drillcores yielded similar $T_{\Delta 47}$ values, ranging from 50 to 155 °C with 87% of samples having $T_{\Delta 47}$ < 100 °C (Fig. 1F and *SI Appendix*, Fig. S3A; all $T_{\Delta 47}$-related data are provided in *SI Appendix*, Tables S1–S3). The two $T_{\Delta 47}$ profiles show generally similar stratigraphic patterns (Fig. 1F), confirming the reproducibility of the $T_{\Delta 47}$ measurements, at least within the Zhangcunping area. Because no geological process is known to reduce $T_{\Delta 47}$ values (7, 23–25), these results suggest that most of our dolomite samples must have formed at temperatures below 100 °C, which is inconsistent with an origin via the widely accepted burial–hydrothermal dolomitization model (5, 7).

We note that the $T_{\Delta 47}$ records from the Zhangcunping drillcores differ from results for Doushantuo dolostones in earlier studies of the Huajipo (23) and Jiulongwan (23, 24) shelf sections in the Yangtze Gorges area (*SI Appendix*, Fig. S1C), which yielded generally low Δ_{47} values that correspond to significantly higher temperatures [up to 224 °C based on the latest calibration (*Methods*)]. These high temperatures are inferred to reflect postdepositional hydrothermal alteration of the host rocks and loss of original Δ_{47} signals (23, 24), thus potentially supporting the burial–hydrothermal dolomitization model for those study sites. The low $T_{\Delta 47}$ values in our drillcores indicate better preservation of original Δ_{47} signatures in the Zhangchunping area. We explore this possibility below.

Evaluation of Secondary Alteration of $T_{\Delta 47}$ Records. Original $T_{\Delta 47}$ signatures are subject to secondary alteration via meteoric diagenesis, recrystallization, and solid-state reordering during geological burial, all of which result in shifts to higher-than-original $T_{\Delta 47}$ values (7, 23–25). Although secondarily altered material could not be completely avoided, we minimized such influences by microdrilling only fine-grained dolostone (i.e., dolomicrite) [grain size: 20 ± 15 μm (mean ± SD, $n = 37$; Fig. 1 A and B] suitable for Δ_{47} analysis (*SI Appendix*, Fig. S4), avoiding the coarse dolomite grains that are typically ascribed to deep burial or high-temperature processes. Meteoric and other fluid-buffered diagenetic processes commonly lead to positive covariation of carbonate carbon and oxygen isotope compositions ($\delta^{13}C$–$\delta^{18}O$) (26). In
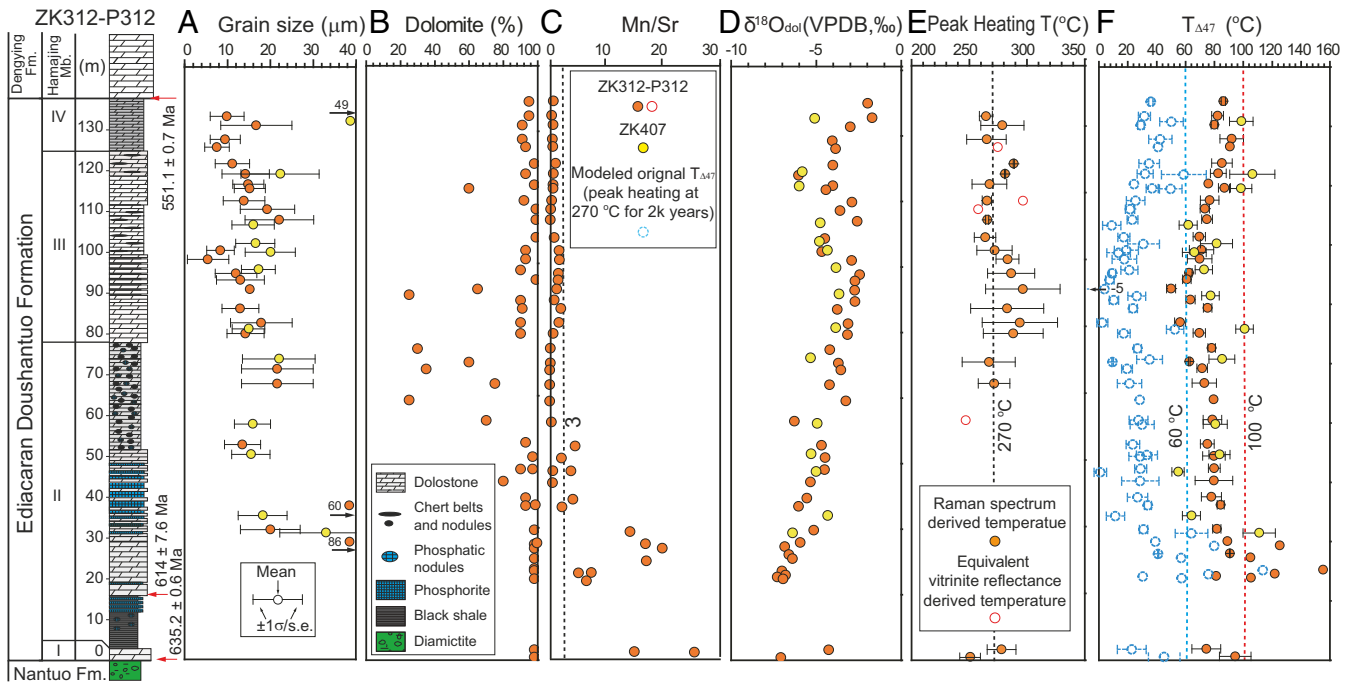
Fig. 1. Clumped-isotope–based paleotemperature ($T_{\Delta 47}$) profile of the Ediacaran Doushantuo Formation dolomites, with paired petrological and geochemical data for evaluation of dolomitic recrystallization, diagenesis, and solid-state reordering, from drillcores ZK407 and ZK312-P312 in Zhangcunping area, Hubei Province, South China. (*A*) Size distributions of dolomite grains. (*B*) Dolomite concentrations. (*C*) Mn/Sr ratios; values <3 indicate insignificant diagenetic alteration (26). (*D*) Oxygen isotopic compositions of dolomite ($\delta^{18}O_{dol}$; parts per thousand relative to Vienna Pee Dee Belemnite [VPDB]). (*E*) Peak heating temperatures (T) derived from Raman spectra and equivalent vitrinite reflectance (eq-R_o) measurements of coexisting OM. The dashed line at 270 °C is the rough average of two peak heating temperature records. (*F*) $T_{\Delta 47}$ records, demonstrating low dolomite-formation temperatures (<100 °C for directly measured $T_{\Delta 47}$ values and <60 °C for modeled values of solid-state reordering effects give an average peak heating temperature of 270 °C for 2,000 y). The data uncertainties are given as SD (σ) for grain size and peak heating temperature or SE (s.e.) for $T_{\Delta 47}$. Dolomite grain size and peak heating temperatures were measured from thin sections, and other data were generated using microdrilled powders. See *Methods* and *SI Appendix* for details. Data sources: lithostratigraphic data for ZK312-P312 are from ref. 22; geochronological data are from refs. 20 and 21. Abbreviations: Fm., Formation; Mb., Member.

contrast, our samples show no significant covariation (r = +0.14 for ZK312-P312) or moderately negative covariation (r = −0.57 for ZK407) (*SI Appendix*, Fig. S5), suggesting that fluid-buffered diagenesis did not significantly affect our studied samples. The degree of fluid-buffered diagenetic alteration of marine carbonates is also commonly assessed using Mn/Sr ratios and $\delta^{18}O$, with values of Mn/Sr < 3 and $\delta^{18}O$ > −10‰ indicative of less altered samples (26). Our samples mostly yielded Mn/Sr < 3 and $\delta^{18}O$ > −7‰, similarly suggesting only limited fluid-buffered diagenetic alteration. However, some samples from the lower parts of the two study cores yielded Mn/Sr >3 (Fig. 1*C* and *SI Appendix*, Table S4) and/or relatively low $\delta^{18}O$ values (down to −7.3‰; Fig. 1*D*), suggesting a

degree of late-stage recrystallization also indicated by microscopic and cathodoluminescence images (*SI Appendix*, Figs. S4 *F and G* and S6). This phase may account for the relatively high $T_{\Delta 47}$ values of some of these samples (Fig. 1*F*).

In order to directly test the effect of secondary alteration on $T_{\Delta 47}$ values, we selected nine samples (eight samples from the study Doushantuo Formation and one sample from overlying Dengying Formation) with different carbonate textures (*SI Appendix*, Table S5). These samples consisted of fine-grained matrix enclosing either coarse-grained dolomite patches or carbonate veins (*SI Appendix*, Fig. S7). Compared with the fine-grained matrix, the coarse-grained dolomite patches and veins show
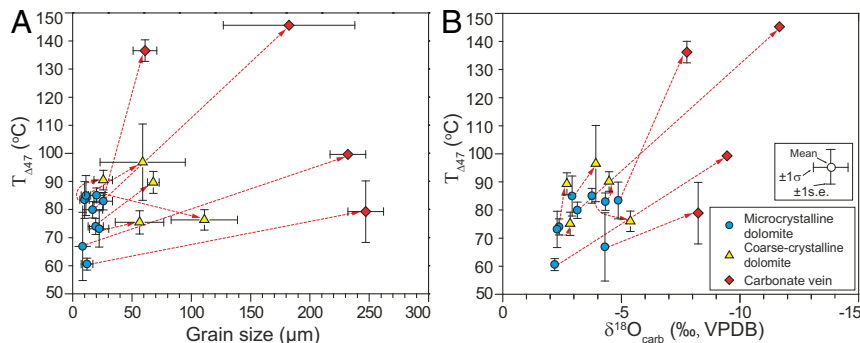

Fig. 2. Cross-plots of $T_{\Delta 47}$ versus grain size (*A*) and $T_{\Delta 47}$ versus $\delta^{18}O_{carb}$ (*B*) for eight samples from study Doushantuo Formation and one sample from overlying Dengying Formation, which have different carbonate textures. The red dashed line, which points away from blue-filled circles to yellow-filled triangle or red-filled diamond, are coded to different textures in the same sample (see legend).

generally larger crystal sizes, lower $\delta^{18}O_{carb}$ values, and higher $T_{\Delta 47}$ values (Fig. 2). These patterns indicate that the fine-grained dolomicrite is the component that was least altered by late diagenesis and the one that potentially best preserves the original $T_{\Delta 47}$ signatures of the study units. Importantly, these sample-scale heterogeneities are inconsistent with wholesale, much later diagenetic resetting of primary geochemical signals.

Modeling of Solid-State Reordering in the Doushantuo Formation. In this discussion, we seek to reconcile our low $T_{\Delta 47}$ values with other evidence suggesting much higher heating temperatures encountered during the long burial history of our samples; this work provides further constraints on our $T_{\Delta 47}$ records. Solid-state reordering of carbonates is a process occurring at elevated temperatures that randomizes primary $^{13}C–^{18}O$ bonds through the exchange of oxygen and/or carbon atoms among carbonate ion groups in the crystal lattice, thus resulting in lower $\Delta 47$ and higher $T_{\Delta 47}$ values (25). The extent of C–O bond reordering is a function of the temperature–time history of a sample (25). Reordering in the Doushantuo study samples is a distinct possibility given that an average peak heating temperature of ~270 °C is suggested both by equivalent vitrinite reflectance (eq-R_o; 247 to 297 °C; Fig. 1E) and Raman spectral measurements of sedimentary organic matter (OM) (251 to 297 °C; Fig. 1E) (see *Methods* for further information about thermal proxies).

To evaluate the influence of solid-state reordering on our $T_{\Delta 47}$ values, we reconstructed the thermal history of the Doushantuo Formation (Fig. 3) based on its regional tectonic history. Additional assumptions are a present-day average Earth surface temperature of 20 °C, a geothermal gradient of 25 °C/km, and an initial temperature of 0 °C during Doushantuo deposition at 635 Ma reflecting the transition from a Cryogenian glacial climate to an Ediacaran greenhouse climate (27). The Doushantuo Formation was deposited in a passive continental margin setting from ~635 to 551 Ma, with subsequent maximum burial depths of ~4 km for platform facies and ~7 km for coeval basinal facies (28). The study succession was uplifted at ~541 Ma as suggested by a regional stratigraphic unconformity in the platform facies (29) and subsequently deformed and thickened by orogenic activity. During the late Silurian and early Devonian, much of the South China Block was uplifted again and exposed to weathering and erosion. Rifting and subsidence began in the middle-late

Devonian, with accumulation of shallow-marine siliciclastics and carbonates from the Late Devonian to the mid-Triassic. During the Mesozoic and Cenozoic, orogenic activity related to the assembly of China caused further uplift and exposure of the study region, resulting in erosional activity that has continued to the present (28). Given a maximum burial depth of 4 km for the platform facies and the tectonic history outlined above, the maximum regional burial temperature of the Doushantuo Formation in the Zhangcunping area was ~100 °C.

The Doushantuo Formation in the study area experienced one or more hydrothermal events that may have played an important role in its overall thermal history (Fig. 3). Carbonate veins in Doushantuo basal cap carbonates (Member I) from the Yangtze Gorges area are direct evidence for such activity, which yielded extremely low $\Delta 47$ values [down to 0.265‰ ($T_{\Delta 47}$ = 476 °C)]. These values have been interpreted as evidence of high-temperature hydrothermal fluids migrating through the cap carbonate and other permeable layers in the Doushantuo Formation (23). This inference is further supported by stratigraphic decreases in illite content (from 94 to 0%) and eq-R_o (from 2.05 to 1.65%) from the cap dolostone to the top of the Doushantuo Formation in the Yangtze Gorges area (30), which are consistent with decreasing temperatures or thermal overprints up-section. These lines of evidence suggest the former existence of a steep thermal gradient in the vicinity of the cap dolostone unit that can be best explained by a hydrothermal event on a short timescale (e.g., thousands of years). A hydrothermal alteration event is also consistent with high-temperature data from our eq-R_o (247 to 297 °C) and Raman spectral measurements (251 to 297 °C) for Doushantuo OM in our study units (Fig. 1E).

The timing of this hydrothermal alteration event is still uncertain but may have been related to a thermal episode in either the mid-Silurian (430 to 425 Ma) or the mid-Late Mississippian (328 to 325 Ma) (30) (Fig. 3). Alternatively, it may have been linked to silica-rich hydrothermal deposits formed during the late Ediacaran and Cambrian (31) (Fig. 3). However, whatever the age of the hydrothermal alteration event(s), their effects on the $T_{\Delta 47}$ values of our study samples through solid-state reordering would have been similar and thus do not affect the modeling results described below.

We used the dolomite-based exchange-diffusion kinetic model of ref. 25 to evaluate the influence of solid-state reordering on our $T_{\Delta 47}$ values (see *Methods* for comparisons with other models). This model allowed us to predict the alteration of $T_{\Delta 47}$ values according to alternative thermal scenarios and, by comparison with $T_{\Delta 47}$ values measured in our study and other thermal records, rule out implausible thermal scenarios. We adopted rate constants for solid-state reordering of dolomite from ref. 32 and assumed an initial temperature for modeled dolomite in the range of 0 to 50 °C, which is a plausible temperature range for carbonate precipitation in Earth surface environments. Using these parameters, a set of models were run in which peak heating temperatures were related to a high-temperature hydrothermal event of unknown duration that occurred during the burial of the Doushantuo Formation in the study area (Fig. 3). In the simulation, we varied the heating duration, peak temperature, heating–cooling rates, or initial temperature while keeping other parameters constant in order to explore possible thermal scenarios for the study units (Fig. 4).

Simulations were first run for a hydrothermal heating event over long timescales (~10^7 y) (Fig. 4A) according to the reconstructed thermal history from 635 Ma to present (Fig. 3). These models assumed an initial temperature of 0 °C and a range of peak heating temperatures (i.e., 125, 155, 185, 215, 245, and 270 °C) with symmetric heating–cooling rates for the hydrothermal event, which was assumed to have occurred over 6×10^7 y beginning at 460 Ma (i.e., during the mid-Silurian as suggested in ref. 30). Our results show that no significant solid-state reordering
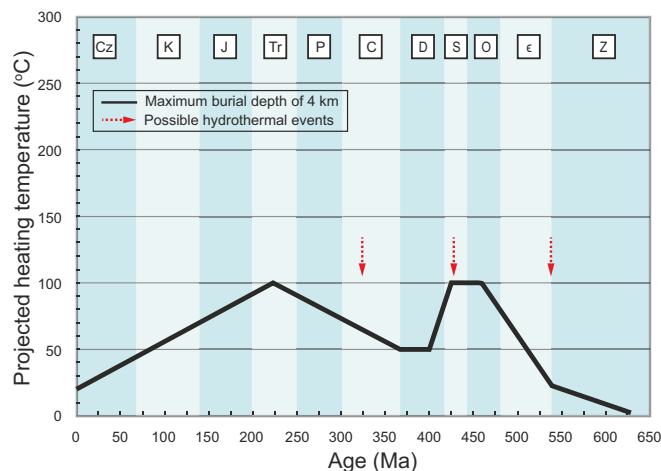

Fig. 3. Model of thermal history of the Doushantuo Formation from 635 Ma to present based on its regional tectonic history outlined in this study. See text for details. C, Carboniferous; Cz, Cenozoic; D, Devonian; ϵ, Cambrian; J, Jurassic; K, Cretaceous; O, Ordovician; P, Permian; S, Silurian; Tr, Triassic; Z, Ediacaran.

is expected for peak temperatures at or below ~155 °C, while partial reordering was observed for peak temperatures between ~155 and 245 °C, which raised final modeled $T_{\Delta47}$ values up to ~90 °C. Importantly, this result suggests that the maximum geothermal heating temperature of 100 °C with a burial depth of 4 km for the platform facies would not have significantly affected the final $T_{\Delta47}$ values of our study samples. In contrast, for peak heating temperatures of >245 °C, the modeled $T_{\Delta47}$ values of the study dolomites would be significantly higher than the measured $T_{\Delta47}$ values of 50 to 106 °C for well-preserved samples in this study. We note that the modeled $T_{\Delta47}$ values will rise correspondingly if we increase the initial temperatures from 0 to 50 °C.

The model results above indicate that the thermal scenarios with peak temperatures of >245 °C and heating durations of >6 × 10^7 y are not viable for our study unit with current symmetric heating–cooling rates. The implication is that the duration of the event must have been much shorter than 6 × 10^7 y for a hydrothermal event with a peak temperature of ~270 °C, as suggested by eq-R_o (247 to 297 °C) and Raman spectral measurements of OM (251 to 297 °C) in the study units (Fig. 1E). We note that at higher temperatures (e.g., >155 °C, as suggested in this model), a reduction in heating duration through changing heating–cooling rates can also yield lower modeled $T_{\Delta47}$ values, but this is equivalent to shortening the hydrothermal event time (see below). Given our model results and the geological evidence for a likely short hydrothermal event (e.g., 10^3 y) with peak heating temperature of ~270 °C (see above), we focus on modeling the hydrothermal heating event at short timescales.

Simulations were further run for the hydrothermal heating event on shorter timescales, i.e., ~10^4 y (Fig. 4B) and ~10^3 y (Fig. 4C). Because insignificant solid-state reordering was observed for peak temperatures at or below ~155 °C (Fig. 4A) and

the maximum burial temperature of the study unit was ~100 °C (see above), we focused only on hydrothermal heating event itself with the peak temperature of 270 °C in these simulations. These models assumed an initial temperature of 0 °C and a peak temperature of 270 °C for intervals of 10^4 y (Fig. 4B) and 2 × 10^3 y (Fig. 4C) with variable heating–cooling rates. We tested seven different heating–cooling rate combinations (cases 1 to 7 in Fig. 4 B and C). Given heating on 10^4-y and 10^3-y timescales, the modeled $T_{\Delta47}$ values vary from 0 to 91 °C (Fig. 4B) and 0 to 68 °C (Fig. 4C), respectively. In these simulations, a shorter heating time at high temperatures generated lower modeled $T_{\Delta47}$ values (Fig. 4 B and C), indicating that a short duration at high temperatures was essential for preservation of low $T_{\Delta47}$ values. Among all tested simulations, the one that best matched our measured $T_{\Delta47}$ values (yielding a modeled $T_{\Delta47}$ of 55 °C compared to 50 °C for the lowest measured $T_{\Delta47}$ value) and other time–temperature history constraints assumes a 2,000-y hydrothermal event with the heating–cooling rates of case 1 (black solid line in Fig. 4C). Based on this simulation, we then varied the initial temperature from 0 to 50 °C, yielding a range of 55 to 99 °C for the final modeled $T_{\Delta47}$ values, which corresponds well to the range of measured $T_{\Delta47}$ values (50 to 106 °C) in our well-preserved samples (Fig. 4D).

We note that other model parameterizations (i.e., alternative combinations of heating duration, heating–cooling rates, and initial temperatures), as well as other solid-state reordering models [e.g., the dolomite-based "transient defect/equilibrium defect" or the "equilibrium defect" models (33, 34)], can also generate modeled $T_{\Delta47}$ values that come close to the low $T_{\Delta47}$ values observed in this study (*SI Appendix*, Fig. S8) We also note that the kinetic parameters upon which these models are based contain intrinsic uncertainties. Therefore, the 2,000-y alteration scenario described above that best matches our $T_{\Delta47}$ data (shown
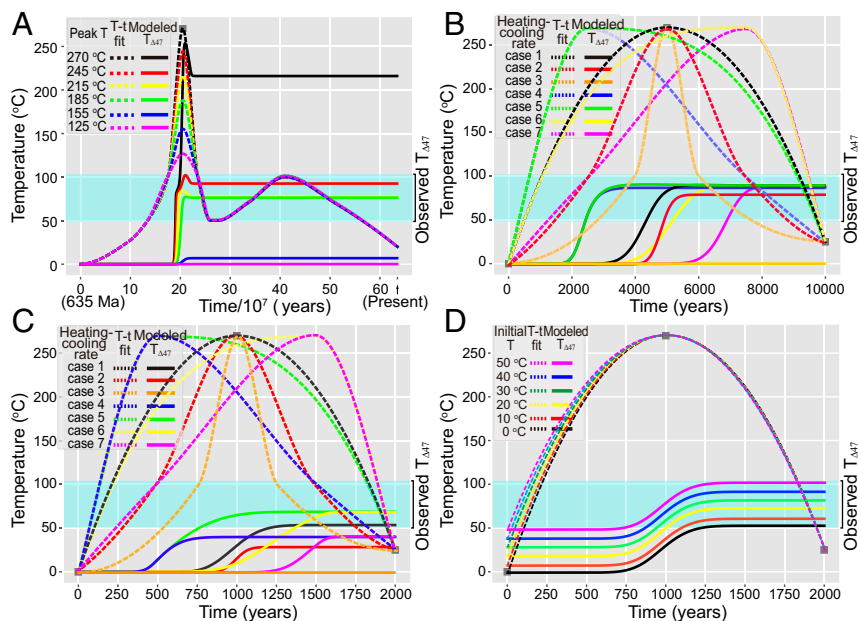
Fig. 4. Solid-state reordering modeling of the study Doushantuo Formation. (*A*) Model results for long-duration (~10^7 y) hydrothermal events. These models assumed an initial temperature of 0 °C and peak temperatures of 125, 155, 185, 215, 245, and 270 °C with symmetric heating–cooling rates over a 6 × 10^7-y interval beginning at 460 Ma. The models were based on the reconstructed thermal history of Fig. 3 from 635 Ma to the present. (*B* and *C*) Model results for short-duration (*B*: ×10^4 y; *C*: ×10^3 y) hydrothermal events. These models assumed an initial temperature of 0 °C, a peak heating temperature of 270 °C for 10,000 y (in *B*) or 2,000 y (in *C*) with variable heating–cooling rates, including three symmetric heating–cooling cases (cases 1 to 3) and four asymmetric heating–cooling cases (cases 4 to 7). (*D*) Model results assuming a varying initial temperature from 0 to 50 °C, a peak temperature of 270 °C for 2,000 y, and a fixed heating–cooling rate (i.e., case 1 in *C*). In all subfigures, the "T-t fit" lines denote assumed heating T-time paths, while the "Modeled $T_{\Delta47}$" lines denote the corresponding $T_{\Delta47}$ evolution of the Doushantuo dolomites predicted by a solid-state reordering model. The shallow blue bands represent the range of measured $T_{\Delta47}$ values of well-preserved Doushantuo dolomites in this study. See *Results and Discussion* for further details.
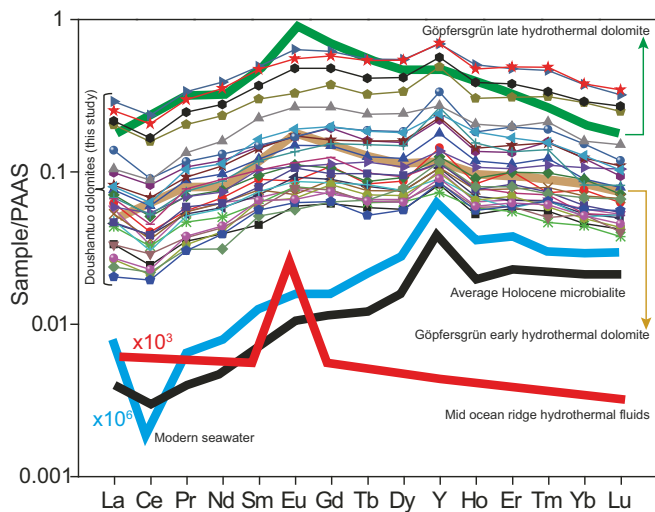
Fig. 5. Rare earth element (REE) and yttrium (Y) patterns of carbonate fractions of Doushantuo Formation dolostones from drillcore ZK312-P312 normalized to post-Archean Australian shale (PAAS). The Doushantuo data are from this study; other data were adopted from ref. 35.

in Fig. 4*D*) should be considered as only one of many possible solutions. However, all of the possible solutions require short heating times at high temperatures in order to generate low modeled $T_{\Delta 47}$ values in combination with a measured average peak temperature of ~270 °C. Based on previous studies of hydrothermal events (23, 30), we prefer a ~10^3-y timescale (e.g., the 2,000-y duration modeled above) for the heating event that affected the Doushantuo Formation. A heating event of this duration is consistent with a transient incursion of hot fluids through tectonically activated deep-seated crustal faults.

Our modeling work can provide further constraints on our $T_{\Delta 47}$ records. The initial $T_{\Delta 47}$ values of our samples can be quantitatively estimated based on the linear relationship between the assumed initial temperatures (i.e., 0 to 50 °C) and corresponding modeled final $T_{\Delta 47}$ values, as presented in the 2,000-y alternation scenario above (Fig. 4*D*). Our results indicate that solid-state reordering in the preferred 2,000-y alteration scenario would have caused an increase in $T_{\Delta 47}$ of 42 to 55 °C, which is consistent with initial $T_{\Delta 47}$ values between 0 and 60 °C, as calculated for 93% of our samples (Fig. 1*F* and *SI Appendix*, Fig. S3*B*). We note that this result is robust to choice of dolomite-based solid-state reordering models; similar results are obtained using the alternative dolomite-based "transient defect/equilibrium defect" or "equilibrium defect" models (33, 34) (*SI Appendix*, Table S1), although in these cases a heating duration of 4,000 to 70,000 y is required at a peak temperature of 270 °C (*SI Appendix*, Fig. S8). These results are consistent with most of the dolomites analyzed in this study having formed at temperatures of <60 °C. An alternative interpretation—that the measured Doushantuo $T_{\Delta 47}$ values have not been raised by solid-state reordering—is only possible if the hydrothermal event was extremely short (<<100 y). We do not consider such rapid heating and cooling geologically feasible. Thus, we consider our modeling results, even in the face of existing uncertainties in the model assumptions, as direct evidence for a low-temperature origin of these dolomites.

Low-Temperature Formation of Massive Doushantuo Dolomites. In order to explore the mechanism of low-temperature formation of the massive Doushantuo dolomites and determine whether they can retain primary seawater information, we analyzed the rare

earth element and yttrium (REE+Y) compositions of our samples. Both the bulk-rock and carbonate fractions of all samples display a positive Y anomaly, a negative cerium (Ce) anomaly, light REE depletion, and lack of a europium (Eu) anomaly (Fig. 5 and *SI Appendix*, Table S4). These features are similar to the REE+Y compositions of modern seawater and Holocene microbialites, which are likely to be similar to the patterns in ancient equivalents (35), but they are distinctly different from those of hydrothermal fluids and related dolomites (summarized in ref. 36). These observations suggest that the Doushantuo dolomites originated from seawater or marine near-surface pore fluids.

Furthermore, we calculated the $\delta^{18}O$ compositions of the diagenetic fluids ($\delta^{18}O_{fluid}$; *SI Appendix*, Table S1) based on our $\delta^{18}O_{dol}$–$T_{\Delta 47}$ data assuming that diagenetic recrystallization of carbonate, if it occurred, was the dominant influence on measured $T_{\Delta 47}$ values. Our $\delta^{18}O_{fluid}$–$T_{\Delta 47}$ data, plotted on a diagram of reference values for modern carbonates and coexisting diagenetic fluids equilibrated over a range of geological conditions (Fig. 6), can be interpreted within the framework of ref. 37. On this basis, the studied unit would appear to have recrystallized primarily in an early-to-late diagenetic, fluid-buffered environment (*SI Appendix*, Fig. S9). However, if a ~6.5‰ depletion of ^{18}O in Ediacaran seawater relative to modern seawater (as modeled by ref. 38) is taken into consideration, the corrected $\delta^{18}O_{fluid}$–$T_{\Delta 47}$ data favor an early-to-late diagenetic, strongly rock-buffered environment for recrystallization (Fig. 6). Furthermore, a restricted marine/evaporite to early diagenetic, strongly rock-buffered environment is indicated if we calculate corrected $\delta^{18}O_{fluid}$ values using the initial $T_{\Delta 47}$ values of our samples (Figs. 1*F* and 6) as derived from the solid-state reordering model and assuming a hydrothermal event with a peak heating of 270 °C for 2,000 y (see above).

Based on the elemental and isotopic observations above, we propose that our Doushantuo dolomites formed during early
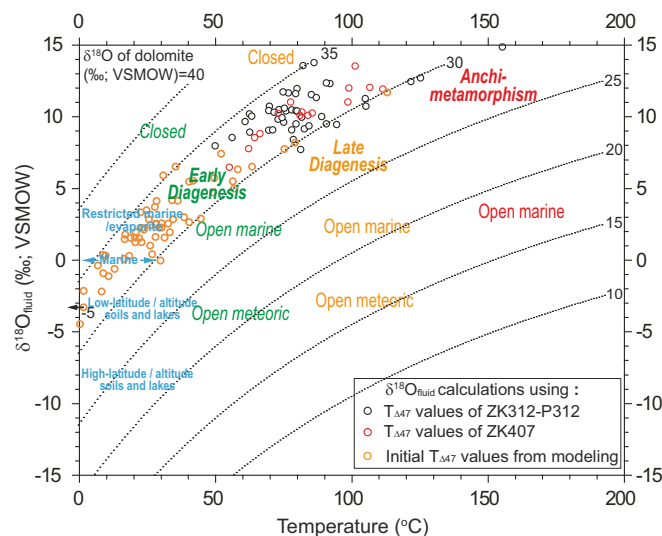

Fig. 6. Calculated $\delta^{18}O$ compositions of the diagenetic fluids ($\delta^{18}O_{fluid}$) versus paired $T_{\Delta 47}$ data for Doushantuo dolomite. Recrystallization environments (colored text: early or late diagenetic or anchi-metamorphic) except for those modern environments in blue texts are either closed (i.e., rock-buffered) or open (i.e., fluid-buffered). Reference isotopic compositions for carbonates and coexisting diagenetic fluids equilibrated over a range of geological conditions were adopted from ref. 36 but updated to the $\delta^{18}O$ compositions of dolomite. All originally calculated $\delta^{18}O_{fluid}$ values were corrected to modern seawater $\delta^{18}O$ by adding +6.5‰ as modeled by ref. 38. The initial $T_{\Delta 47}$ values from modeling are based on a solid-state reordering model assuming a hydrothermal event with a peak heating of 270 °C for 2,000 y. See *Methods* for further explanation of calculations and *Results and Discussion* for detailed interpretations.

diagenesis. It is possible that they first precipitated from seawater or marine porewaters as calcitic and/or aragonitic muds that were then neomorphosed to dolomite in a rock-buffered environment in the presence of Mg-rich pore fluids typical of an evaporitic setting (e.g., the sabkha model) (1). Indeed, paleogeographic reconstructions suggest that shallow-water facies of the Doushantuo Formation were deposited in a semirestricted shelf lagoon (39) at a paleolatitude of ~30 °N (19).

It is also possible that the Doushantuo dolomites first precipitated from seawater or marine porewaters as nonstoichiometric and disordered proto-dolomite or very high-Mg calcites through microbial mediation (and associated OM) and that they were subsequently transformed to ordered dolomite during early burial (i.e., the organogenic dolomite model) (12–15). Microbial nonstoichiometric and disordered proto-dolomite typically precipitates from seawater

as spherical or ellipsoidal crystals with diameters of tens of micrometers (15, 40) (Fig. 7A). The Doushantuo dolomite consists of many similar-sized spherical to ellipsoidal crystals (Fig. 7B), consistent with a possible microbial origin. Raman spectroscopy showed that both spherulitic and nonspherulitic dolomitic crystals are surrounded by OM and apatite (Fig. 7 C and D), both of which are linked to biological processes (41). Additional petrological observations of our samples under a scanning electron microscope (SEM) revealed well-preserved microbial fossils (Fig. 7E) and abundant mycelia and mycetomes associated with OM (Fig. 7F), also suggesting intense microbial activity. This activity may have served to catalyze the early-stage formation of the Doushantuo dolomite.

The early-stage formation of organogenic dolomite commonly exhibits weak to no cationic ordering, although it may have a Mg/Ca ratio close to 1:1 (5). However, as reported for many
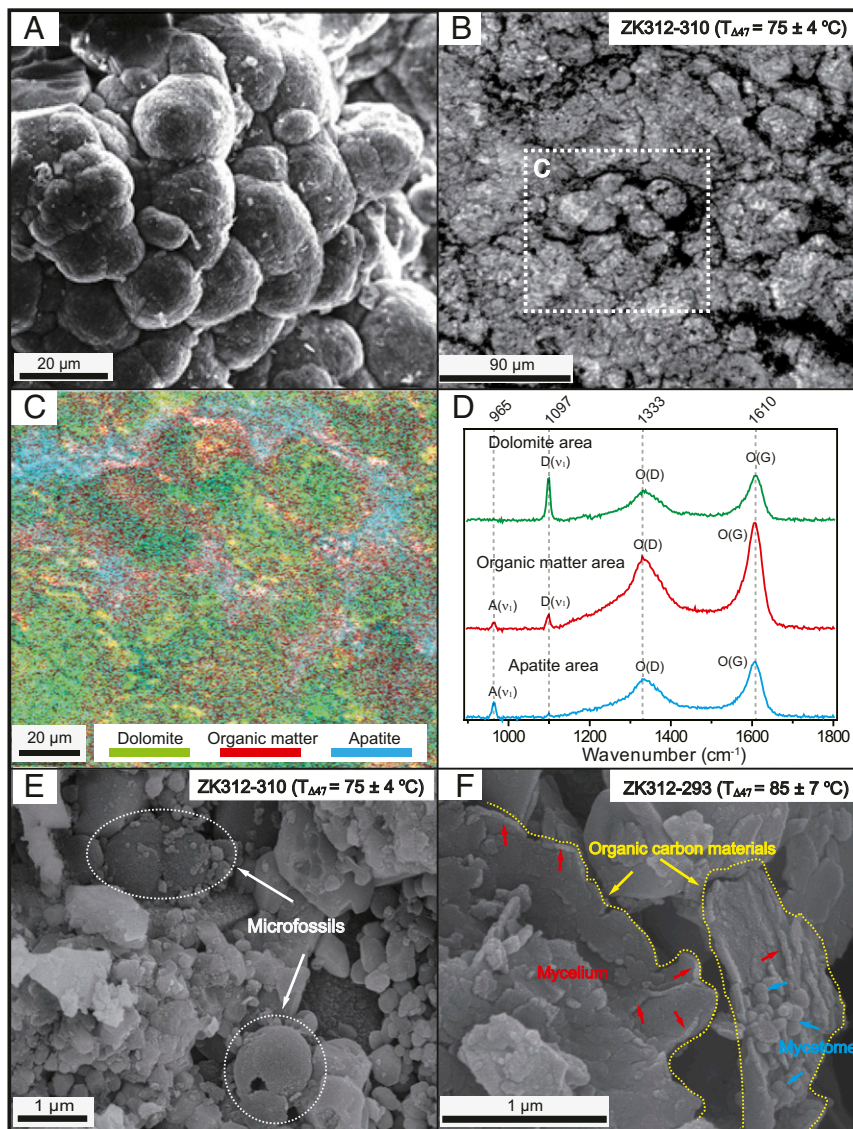
Fig. 7. Petrological characteristics of laboratory-synthesized microbial dolomites and Doushantuo dolomites from drillcore ZK312-P312. (*A*) Spherulitic grains of microbial dolomite. Republished with permission of Geological Society of America, from ref. 40; permission conveyed through the Copyright Clearance Center Inc. (*B*) Spherulitic grains of Doushantuo dolomites in a typical sample (ZK312-310), which yielded a clumped-isotope–based paleotemperature ($T_{\Delta47}$) of 75 ± 4 °C. (*C*) Raman filter map of selected area in *B* showing distribution of dolomite (green), surrounded by OM (red) and apatite (blue). (*D*) Selected average Raman spectra from *C* showing close association between dolomite [diagnostic peak D(ν_1)], OM [diagnostic peaks O(D) and O(G)], and apatite [diagnostic peak A(ν_1)]. (*E*) Well-preserved microfossils of a typical sample (ZK312-310). (*F*) Well-preserved OM associated with abundant mycelia and mycetomes in a typical sample (ZK312-293), which yielded a $T_{\Delta47}$ of 85 ± 7 °C. Note: Photo in *B* is a transmitted-light petrographic image and photos in *A*, *E*, and *F* are SEM images.

Precambrian dolostones (42, 43), the Doushantuo Formation contains fully ordered dolomite characterized by the presence of a diagnostic d(015) peak in X-ray diffraction spectra (*SI Appendix*, Fig. S10). The most likely interpretation is that the formation of disordered nonstoichiometric proto-dolomites or very high-Mg calcites was followed by gradual cationic ordering in a rock-buffered environment, as observed under both shallow and slightly deep burial conditions (12, 14, 15).

Other early diagenetic mechanisms are also possible, but the two early diagenetic mechanisms outlined above agree well with our isotopic and elemental observations and are further supported by the mainly fine-grained dolomicritic nature of the Doushantuo dolostones (*SI Appendix*, Figs. S4, S6, and S7). The presence of dolomicrite points to a diagenetic environment characterized by highly oversaturated porewaters and the nucleation and precipitation of large numbers of small xenotopic dolomite crystals (14).

Summary and Implications. Our $T_{\Delta 47}$ records along with cogenerated elemental, isotopic, and petrographic data indicate that the massive ordered dolomites of the Ediacaran Doushantuo Formation formed in a low-temperature early-diagenetic environment with seawater-derived fluids and abundant microbial activity. These features are consistent with modern early diagenetic dolomitization models. Most likely, the sedimentary precursors of the Doushantuo dolomites (e.g., calcite, aragonite, very high-Mg calcite, or nonstoichiometric and disordered proto-dolomite) precipitated from seawater or marine porewaters and were subsequently transformed to ordered dolomites during early diagenesis in a shallow-burial porewater setting. Therefore, our study provides direct evidence for massive early-diagenetic dolomite formation in Precambrian oceans. This result implies that early diagenetic dolomitization models for modern settings may be relevant to massive Paleozoic and Precambrian dolomite deposits in addition to the widely accepted burial–hydrothermal dolomitization model. Furthermore, the so-called "dolomite problem" may be a product of specific conditions common if not persistent in Paleozoic and Precambrian oceans.

Our findings also have important implications for the environmental relevance of some carbonate-hosted geochemical proxies widely used in deep-time research, such as $\delta^{13}C_{carb}$ and REEs. Although early diagenetic processes (e.g., organic oxidation and sulfate reduction) likely affected the chemical and isotopic compositions of porewaters, we conclude that overprints of original marine carbonate signatures via these diagenetic effects were limited. Specifically, retention of the chemical and isotopic compositions of the carbonate precursors were favored by rock buffering facilitated by microscale dissolution–reprecipitation processes during early diagenetic recrystallization (44, 45). In addition, sediment porewaters tend to share many chemical and isotopic properties with overlying seawater, particularly in organic-lean sediments, such as those of the studied Doushantuo dolostones, which have low total organic carbon contents (0.37 ± 0.09% [mean ± 1 SE; $n = 29$; *SI Appendix*, Table S4) (22). These conditions may explain why our REE+Y data reflect a seawater signal, and why the $\delta^{13}C_{carb}$ values of the Doushantuo and other coeval dolomitic successions were able to capture large perturbations of the oceanic carbon cycle during the Ediacaran (46). As such, ancient dolostones can be important archives of conditions in the early oceans, and future research should focus further on the particular conditions in the early oceans that episodically or persistently favored widespread early dolomitization.

Methods

Samples and Rock Powder Sampling. Forty-five samples from the Doushantuo Formation at ZK312-P312 were prepared for petrological, isotopic, elemental, and mineralogical analyses. Fifteen samples from the Doushantuo Formation at ZK407 were analyzed for isotopic and dolomitic grain size

characteristics in order to confirm the reproducibility of measurements from ZK312-P312. Rock powders for isotopic, elemental, and mineralogical analyses were collected from core slabs using a hand-held carbide microdrill (bit diameter, 0.7 to 1.0 mm). Prior to microdrilling, the intended sampling points were examined in thin sections (ca. 2.5 × 4 cm) to avoid areas of visible late diagenetic alternation. We targeted only microcrystalline areas that best represent the "primary" phases of the study dolomites.

Isotope Analyses and $T_{\Delta 47}$ Calculation. The Δ_{47} analysis was carried out in duplicate at the University of California, Los Angeles (UCLA), and in State Key Laboratory of Geological Processes and Mineral Resources at China University of Geosciences–Wuhan (CUG-W) to monitor the reproducibility of our results. A detailed description of the Δ_{47} method used at UCLA can be found in ref. 24. The results from both laboratories show almost the same values and the same trend (*SI Appendix*, Fig. S11 and Table S2), confirming the reliability of our Δ_{47} data. Both laboratories used a sample preparation line and a MAT253 isotopic ratio mass spectrometer (IRMS) equipped with dual inlet system. Briefly, an aliquot of 10 to 20 mg of rock powder (>200 mesh) was digested in 102 to 105% phosphoric acid at 90 °C, and the resulting CO_2 gas was purified by passing through multiple cryogenic traps, including a Porapak-Q gas chromatograph column held at −20 °C. The main methodological difference between the UCLA and CUG-W laboratories relates to the sample gas preparation line: At UCLA, a custom-built, automated online device purified the CO_2 gas and introduced it to the mass spectrometer, whereas at CUG-W, a manual off-line device was used to purify CO_2 gas and a finger tube was used to transfer gas to the mass spectrometer. The manual off-line device at CUG-W consists of 1) U-shaped cryogenic glass traps for the purification and collection of CO_2 and removal of water and other gases with low vapor pressures (i.e., using liquid nitrogen for collecting CO_2 at −196 °C and a mixture of liquid nitrogen and alcohol for releasing CO_2 at −78 to −90 °C), 2) a U-shaped cryogenic glass trap (length, ~30 cm) packed with 80 to 100 Mesh Porapak Q and a mixture of liquid nitrogen and ethylene glycol (−20 °C) to further purify CO_2 by removing organic contaminants and sulfides, and 3) a final set of glass traps to confine CO_2 in a finger tube using the same two liquids as in step 1 followed by transfer of the purified gas to the mass spectrometer for measurement.

The purified CO_2 gas was analyzed on a specially modified Thermo MAT253 IRMS for measuring $\delta^{18}O$ and clumped isotopes of CO_2. $\delta^{18}O$ values were calibrated relative to the international reference standard NBS-19 ($\delta^{18}O = -2.20‰$) and Chinese national standard GBW04416 ($\delta^{18}O = -11.59 \pm 0.11‰$) and are expressed in standard δ-notation as per mille deviations from the Vienna Pee Dee Belemnite (VPDB) international standard with a precision of better than ±0.1‰ based on duplicate analyses of GBW04416 and selected study samples. The IRMS was configured and operated specifically for clumped-isotope analysis, as described in refs. 47 and 48. Each sample or standard analysis was performed for 10 acquisitions with eight cycles, and each sample was measured two to five times. Nonlinearity corrections were made per standard protocols using water-equilibrated (10, 25, and 50 °C) and heated (1,000 °C) CO_2 gases, as described in ref. 49.

Clumped-isotope values are reported in Δ_{47} notation, representing the per mille enrichment of $^{13}C^{18}O^{16}O$ produced during acid digestion of samples relative to the amount expected for a random distribution of isotopes among all CO_2 isotopologues (18). Specifically, Δ_{47} is calculated as follows:

$$\Delta_{47} = \frac{R^{47}}{2R^{13}R^{18} + 2R^{17}R^{18} + R^{13}(R^{17})^2} - \frac{R^{46}}{2R^{18} + 2R^{13}R^{17} + R^{13}(R^{17})^2} - \frac{R^{45}}{R^{13} + 2R^{17}} + 1,$$

where R refers to the ratio of the minor to the major isotopologues.

All Δ_{47} values are reported on the absolute reference frame (ARF), which was calculated using CO_2 reference gases equilibrated at 10, 25, 50, and 1,000 °C (49). Due to the possible large uncertainties related to Assonov ^{17}O calibration parameters (50–53), we calculated raw Δ_{47} values using the ^{17}O calibration parameters reported in ref. 53, which have been shown to improve interlaboratory data consistency (54). The raw Δ_{47} data were calibrated to the ARF, including application of a fractionation factor of +0.082‰ to account for acid digestion at 90 °C (55), and were further calibrated using the new Δ_{47} values of ETH standards (ETH-1, 0.258‰; ETH-2, 0.256‰; ETH-3, 0.691‰; and ETH-4, 0.507‰) reported in ref. 54. Typical sample precision of the Δ_{47} data based on replicate measurements of our dolomite samples is 0.010‰ (1 SE). Currently, there is some uncertainty regarding the appropriate value of the acid fractionation factor to use for dolomitic samples (e.g., +0.082‰ is reported in ref. 55 and +0.153‰ in ref. 56). We used an acid fractionation factor of +0.082‰ to calibrate our data

because this value has been reproduced in several studies and is widely accepted (48, 55, 57, 58).

Currently published empirical calibration equations (Δ_{47}-low temperature, 1 to 65 °C) have mostly been based on biogenic carbonates and inorganic synthetic calcites (18, 49, 59–61), and only two Δ_{47}-temperature calibration equations for dolomite samples have been reported (50, 62). Because the temperature calibration of ref. 62 was based on only five samples exhibiting a modest correlation ($R^2 = 0.864$), we used the calibration of ref. 50, which is based on 12 samples exhibiting a stronger correlation ($R^2 = 0.997$). However, the temperature calibration of ref. 50 was not converted to the Brand parametric framework and also not normalized to the new values of the ETH standards reported in ref. 54. Because these differences have the potential to cause significant laboratory-specific bias between ref. 50 and our study (58), we minimized this bias by using the international standard NBS-19 to normalize our data and to make them compatible with the temperature calibration of ref. 50. The Δ_{47} value of the NBS-19 international standard (0.378‰) that we used to correct our data (both UCLA and CUG) is 0.024‰ lower than the reported Δ_{47} value of 0.402‰ for NBS-19 in ref. 50. Therefore, we revised the temperature calibrations for dolomite reported in ref. 50 as follows:

$$\Delta_{47} = \frac{0.0428 \times 10^6}{T_{\Delta 47}^2} + 0.1174 - 0.024,$$

where $T_{\Delta 47}$ is temperature in degrees kelvin.

The preceding interlaboratory bias correction of the temperature calibration for dolomites based on a single standard may not be optimal, but it is still better for Δ_{47} temperature calculations than direct use of the original calibration in ref. 50, which is not given in the Brand parametric framework nor calibrated to the ETH standard values reported in ref. 53. We note that the original temperature calibration of ref. 50 yields $T_{\Delta 47}$ values that are only 10 to 24 °C higher than those based on our revised temperature calibration (SI Appendix, Table S1). Furthermore, if we use the calcite-based temperature calibration reported in ref. 61, in which compiled data were derived from representative clumped-isotope calibration studies, or in ref. 54, which is given in the Brand parametric framework and which has been calibrated to the ETH standard values, the calculated $T_{\Delta 47}$ values of our samples are higher by only 16 to 37 °C and 3 to 5 °C, respectively, relative to our revised dolomite temperature calibration (SI Appendix, Table S1). These small differences in calculated $T_{\Delta 47}$ values indicate that use of other (i.e., inferior) temperature calibrations does not affect our conclusion that Doushantuo dolomites must have formed at near-surface temperatures.

Calculation of $\delta^{18}O$ Values of Diagenetic Fluids ($\delta^{18}O_{fluid}$). Fluid O-isotope compositions ($\delta^{18}O_{fluid}$) were calculated by applying measured $T_{\Delta 47}$ values or modeled initial $T_{\Delta 47}$ values and dolomite $\delta^{18}O$ ($\delta^{18}O_{dol}$) of our Doushantuo samples (see text) to the equations of dolomite–oxygen isotope fractionation factor between dolomite and water [$\alpha_{dolomite-water} = (1,000 + \delta^{18}O_{dol})/(1,000 + \delta^{18}O_{fluid})$] and the dolomite–water oxygen isotope fractionation [$1,000\ln\alpha_{dolomite-water} = (2.73 \times 10^6) T^{-2} + 0.26$] reported in ref. 40. Here, T represents the dolomite formation temperature in kelvin degrees, and $\delta^{18}O_{dol}$ values are reported in per mille compared to the Vienna Standard Mean Ocean Water.

Elemental Analysis. For elemental analysis, an aliquot of each sample (ca. 50 mg) was prepared using a standard HNO_3-HF digestion. The digestion step includes progressive acid treatments [HNO_3-HF (1:1) and HNO_3] at 190 °C in a 15-mL Teflon bomb equipped with a screw cap until a complete digestion was achieved. Distilled HNO_3 and trace metal-grade HF reagents were used. Following an evaporation procedure to remove concentrated acid, the sample was diluted with 2% HNO_3. Elemental concentrations were measured on an Agilent 7500a inductively coupled plasma mass spectrometer. Four US Geological Survey (USGS) standards (AGV-2, BHVO-2, BCR-2, and RGM-1) were run with the samples to monitor the analytical accuracy and precision. Analytical errors are better than ±6.1% for Mn, ±0.7% for Sr, and ±8.9% for REE based on duplicate analyses of four USGS standards (AGV-2, BHVO-2, BCR-2, and RGM-2). The SDs for replicate analyses of ZK312-317 and ZK312-368 are better than ±4.6 ppm for Mn, ±1.1 ppm for Sr, and ±0.07 ppm for REEs. REE concentrations were normalized to the post-Archean Australian shale (PAAS) standard (63). REE concentrations in the carbonate fraction were calculated as $X_{Sample} \times (1 - Th_{Sample}/Th_{PAAS})$, where X represents the concentration of the element of interest.

Grain Size Measurement. To measure dolomite grain size in a sample, thin sections were used for microimaging under an electron microscope (10 pictures per thin section). We used Photoshop software to measure grain size (30

points per picture; in total, 300 points). The grain size of each sample was determined as the mean of a 300-point count.

X-Ray Diffraction Measurement. The mineralogy of the powdered samples was determined via X-ray diffraction (Panaco X'Pert PRO DY2198). The study samples consist almost entirely of ordered dolomite (SI Appendix, Fig. S10 and Table S1).

Equivalent Vitrinite Reflectance and Related Peak Heating Temperature Calculation. Thin sections were used for marine vitrinite reflectance ($R_{o,\,mv}$) measurements, which were conducted by microphotometry (CRAIC 20/20 PV) at the Chinese Academy of Geological Sciences, National Research Center of Geoanalysis in Beijing. Equivalent vitrinite reflectance (eq-R_o) is calculated based on $R_{o,\,mv}$ by using the equation (eq-$R_o = 0.618R_{o,\,mv} + 0.4$), as reported by ref. 64. The peak heating temperature was calculated based on eq-R_o using the equation ($\ln[eq$-$R_o] = 0.0078T_{max} - 1.2$), as reported in ref. 65.

Raman Imaging. Micro-Raman spectroscopy was conducted on petrographic targets within the polished thin sections using a WiTec alpha300R confocal Raman imaging microscope with a 532-nm wavelength laser operating at a power between 0.1 and 6 mW, depending on the target. Raman spectra and hyperspectral scans were obtained at variable magnifications of 20× to 100× depending on objectives and, hence, at variable spatial resolutions of up to 360 nm; spectral resolutions of 4 cm^{-1} were achieved using a 600 lines per millimeter grating. Hyperspectral images were created for specific mineral phases using peak intensity mapping for characteristic peaks of each scanned mineral. Average spectra were calculated by creating a mask on homogeneous pixels of individual phases, with subtraction of backgrounds fitted to a polynomial function. Peak parameters were calculated from a Lorenz function modeled for each selected peak. Cosmic ray reduction was applied to all Raman spectra.

Raman Spectrum-Derived Peak Heating Temperature. The average Raman spectra of OM were deconvolved into several peaks (SI Appendix, Fig. S12) using the computer program WITec Project 5 (Gaussian Lorentzian Sum) with a high-fit degree ($R^2 > 0.99$). The Raman spectrum is composed of first-order (1,000 to 1,800 cm^{-1}) and second-order (2,500 to 3,100 cm^{-1}) regions (66). The first-order region is associated with up to five discriminative bands for OM (G, D1, D2, D3, and D4; SI Appendix, Fig. S12) (67). We used the full width at half-maximum (FWHM) of several disordered bands (D1-band and D2-band) to calculate the peak heating temperature [T_{D1}(°C) = −2.15 × (FWHM-D1) + 478 and T_{D2}(°C) = −6.78 × (FWHM-D2) + 535] (67). The peak heating temperature of a sample is reported as the average of T_{D1} and T_{D2}.

SEM. SEM in secondary electron imaging mode was used to characterize the morphology and composition of selected targets, which were also characterized by energy-dispersive X-ray spectroscopy (EDS). Analyses were carried out using a Hitachi SU8010 and a Quanta 450 FEG SEM at CUG-W. Standard operating conditions for SEM imaging and EDS analysis were 10- to 20-kV accelerating voltage, a working distance of 10 mm, and an electron beam current of 1 nA. Samples were coated with a layer of Au to a thickness of a few nanometers prior to analysis.

Data Availability. All data used in this manuscript are provided in SI Appendix.

1. J. Warren, Dolomite: Occurrence evolution and economically important associations. *Earth Sci. Rev.* **52**, 1–81 (2000).

2. R. K. Given, B. H. Wilkinson, Dolomite abundance and stratigraphic age, constraints on rates and mechanisms of Phanerozoic dolostone formation. *J. Sediment. Res.* **57**, 1068–1078 (1987).

3. J. D. Rodriguez-Blanco, S. Shaw, L. G. Benning, A route for the direct crystallization of dolomite. *Am. Mineral.* **100**, 1172–1181 (2015).

4. F. Lippmann, "Sedimentary carbonate minerals" in *Minerals, Rocks and Inorganic Materials* (Monograph Series of Theoretical and Experimental Studies, Springer, Berlin, 1973), vol. 6, p. 228.

5. J. M. Gregg, D. L. Bish, S. E. Kaczmarek, H. G. Machel, C. Hollis, Mineralogy, nucleation and growth of dolomite in the laboratory and sedimentary environment: A review. *Sedimentology* **62**, 1749–1769 (2015).

6. J. A. McKenzie, C. Vasconcelos, Dolomite Mountains and the origin of the dolomite rock of which they mainly consist: Historical developments and new perspectives. *Sedimentology* **56**, 205–219 (2009).

7. U. Ryb, J. M. Eiler, Oxygen isotope composition of the Phanerozoic ocean and a possible solution to the dolomite problem. *Proc. Natl. Acad. Sci. U.S.A.* **115**, 6602–6607 (2018).

8. A. M. Shuster, M. W. Wallace, A. van Smeerdijk Hood, G. Jiang, The Tonian Beck Spring Dolomite: Marine dolomitization in a shallow, anoxic sea. *Sediment. Geol.* **368**, 83–104 (2018).

9. L. S. Land, The origin of massive dolomite. *J. Geol. Educ.* **33**, 112–125 (1985).

10. C. Vasconcelos, J. A. McKenzie, R. Warthmann, S. M. Bernasconi, Microbial mediation as a possible mechanism for natural dolomite formation at low temperatures. *Nature* **377**, 220–222 (1995).

11. X. Qiu, H. Wang, Y. Yao, Y. Duan, High salinity facilitates dolomite precipitation mediated by Haloferax volcanii DS52. *Earth Planet. Sci. Lett.* **472**, 197–205 (2017).

12. S. H. Nordeng, D. F. Sibley, Dolomite stoichiometry and Ostwald's step rule. *Geochim. Cosmochim. Acta* **58**, 191–196 (1994).

13. T. M. Smith, S. L. Dorobek, Alteration of early-formed dolomite during shallow to deep burial: Mississippian Mission Canyon Formation, central to southwestern Montana. *Geol. Soc. Am. Bull.* **105**, 1389–1399 (1993).

14. A. Geske et al., Impact of diagenesis and low grade metamorphism on isotope ($\delta 26Mg$, $\delta 13C$, $\delta 18O$ and 87Sr/86Sr) and elemental (Ca, Mg, Mn, Fe and Sr) signatures of Triassic sabkha dolomites. *Chem. Geol.* **332–333**, 45–64 (2012).

15. A. Bahniuk et al., Characterization of environmental conditions during microbial Mg-carbonate precipitation and early diagenetic dolomite crust formation: Brejo do Espinho, Rio de Janeiro, Brazil. *Geol. Soc. London Spec. Publ.* **418**, 243–259 (2015).

16. I. Fruth, R. Scherreiks, Hauptdolomit (Norian)—stratigraphy, paleogeography and diagenesis. *Sediment. Geol.* **32**, 195–231 (1982).

17. R. A. Wood, A. Y. Zhuravlev, S. S. Sukhov, M. Zhu, F. Zhao, Demise of Ediacaran dolomitic seas marks widespread biomineralization on the Siberian Platform. *Geology* **45**, 27–30 (2017).

18. P. Ghosh et al., $^{13}C–^{18}O$ bonds in carbonate minerals: A new kind of paleothermometer. *Geochim. Cosmochim. Acta* **70**, 1439–1456 (2006).

19. S. Zhang et al., New paleomagnetic results from the Ediacaran Doushantuo Formation in South China and their paleogeographic implications. *Precambrian Res.* **259**, 130–142 (2015).

20. D. Condon et al., U-Pb ages from the neoproterozoic Doushantuo Formation, China. *Science* **308**, 95–98 (2005).

21. P. Liu, C. Yin, L. Gao, F. Tang, S. Chen, New material of microfossils from the Ediacaran Doushantuo Formation in the Zhangcunping area, Yichang, Hubei Province and its zircon SHRIMP U-Pb age. *Chin. Sci. Bull.* **54**, 1058–1064 (2009).

22. C. Li et al., Uncovering the spatial heterogeneity of Ediacaran carbon cycling. *Geobiology* **15**, 211–224 (2017).

23. T. F. Bristow, M. Bonifacie, A. Derkowski, J. M. Eiler, J. P. Grotzinger, A hydrothermal origin for isotopically anomalous cap dolostone cements from South China. *Nature* **474**, 68–71 (2011).

24. S. J. Loyd et al., Evolution of Neoproterozoic Wonoka–Shuram Anomaly-aged carbonates: Evidence from clumped isotope paleothermometry. *Precambrian Res.* **264**, 179–191 (2015).

25. D. A. Stolper, J. M. Eiler, The kinetics of solid-state isotope-exchange reactions for clumped isotopes: A study of inorganic calcites and apatites from natural and experimental samples. *Am. J. Sci.* **315**, 363–411 (2015).

26. A. J. Kaufman, A. H. Knoll, Neoproterozoic variations in the C-isotopic composition of seawater: Stratigraphic and biogeochemical implications. *Precambrian Res.* **73**, 27–49 (1995).

27. P. F. Hoffman, A. J. Kaufman, G. P. Halverson, D. P. Schrag, A neoproterozoic snowball earth. *Science* **281**, 1342–1346 (1998).

28. G. Jiang, M. J. Kennedy, N. Christie-Blick, H. Wu, S. Zhang, Stratigraphy, sedimentary structures, and textures of the Late Neoproterozoic Doushantuo cap carbonate in South China. *J. Sediment. Res.* **76**, 978–995 (2006).

29. M. Y. Zhu, Cambrian integrative stratigraphy and timescale of China. *Sci. China Earth Sci.* **48**, 1–40 (2019).

30. A. Derkowski et al., Hydrothermal alteration of the Ediacaran Doushantuo Formation in the Yangtze Gorges area (South China). *Geochim. Cosmochim. Acta* **107**, 279–298 (2013).

31. D. Chen, J. Wang, H. Qing, D. Yan, R. Li, Hydrothermal venting activities in the Early Cambrian, South China: Petrological, geochronological and stable isotopic constraints. *Chem. Geol.* **258**, 168–181 (2009).

32. M. K. Lloyd, U. Ryb, J. M. Eiler, Experimental calibration of clumped isotope reordering in dolomite. *Geochim. Cosmochim. Acta* **242**, 1–20 (2018).

33. B. H. Passey, G. A. Henkes, Carbonate clumped isotope bond reordering and geospeedometry. *Earth Planet. Sci. Lett.* **351–352**, 223–236 (2012).

34. G. A. Henkes et al., Temperature limits for preservation of primary calcite clumped isotope paleotemperatures. *Geochim. Cosmochim. Acta* **139**, 362–382 (2014).

35. G. E. Webb, B. S. Kamber, Rare earth elements in Holocene reefal microbialites: A new shallow seawater proxy. *Geochim. Cosmochim. Acta* **64**, 1557–1565 (2000).

36. A. P. Nutman, C. R. L. Friend, V. C. Bennett, D. Wright, M. D. Norman, ≥3700 Ma premetamorphic dolomite formed by microbial mediation in the Isua supracrustal belt (W. Greenland): Simple evidence for early life? *Precambrian Res.* **183**, 725–737 (2010).

37. J. M. Eiler, Paleoclimate reconstruction using carbonate clumped isotope thermometry. *Quat. Sci. Rev.* **30**, 3575–3588 (2011).

38. J. B. D. Jaffrés, G. A. Shields, K. Wallmann, The oxygen isotope evolution of seawater: A critical review of a long-standing controversy and an improved geological water cycle model for the past 3.4 billion years. *Earth Sci. Rev.* **83**, 83–122 (2007).

39. G. Jiang, X. Shi, S. Zhang, Y. Wang, S. Xiao, Stratigraphy and paleogeography of the Ediacaran Doushantuo Formation (ca. 635–551Ma) in South China. *Gondwana Res.* **19**, 831–849 (2011).

40. C. Vasconcelos, J. A. McKenzie, R. Warthmann, S. M. Bernasconi, Calibration of the $\delta^{18}O$ paleothermometer for dolomite precipitated in microbial cultures and natural environments. *Geology* **33**, 317–320 (2005).

41. C. Ohtsuki, H. Kushitani, T. Kokubo, S. Kotani, T. Yamamuro, Apatite formation on the surface of Ceravital-type glass-ceramic in the body. *J. Biomed. Mater. Res.* **25**, 1363–1370 (1991).

42. M. E. Tucker, Precambrian dolomites: Petrographic and isotopic evidence that they differ from Phanerozoic dolomites. *Geology* **10**, 7–12 (1982).

43. A. S. Hood, M. W. Wallace, R. N. Drysdale, Neoproterozoic aragonite-dolomite seas? Widespread marine dolomite precipitation in Cryogenian reef complexes. *Geology* **39**, 871–874 (2011).

44. J. M. Gregg, S. A. Howard, S. J. Mazzullo, Early diagenetic recrystallizationof Holocene (<3000 years old) peritidal dolomites, Ambergris Cay, Belize. *Sedimentology* **39**, 143–160 (1992).

45. G. S. Nascimento et al., Oceanographic and sedimentological influences on carbonate geochemistry and mineralogy in hypersaline coastal lagoons, Rio de Janeiro state, Brazil. *Limnol. Oceanogr.* **64**, 2605–2620 (2019).

46. J. P. Grotzinger, D. A. Fike, W. W. Fischer, Enigmatic origin of the largest-known carbon isotope excursion in Earth's history. *Nat. Geosci.* **4**, 285–292 (2011).

47. K. W. Huntington et al., Methods and limitations of "clumped" CO_2 isotope (Δ_{47}) analysis by gas-source isotope ratio mass spectrometry. *J. Mass Spectrom.* **44**, 1318–1329 (2009).

48. B. H. Passey, N. E. Levin, T. E. Cerling, F. H. Brown, J. M. Eiler, High-temperature environments of human evolution in East Africa based on bond ordering in paleosol carbonates. *Proc. Natl. Acad. Sci. U.S.A.* **107**, 11245–11249 (2010).

49. K. J. Dennis, H. P. Affek, B. H. Passey, D. P. Schrag, J. M. Eiler, Defining an absolute reference frame for "clumped" isotope studies of CO_2. *Geochim. Cosmochim. Acta* **75**, 7117–7131 (2011).

50. M. Bonifacie et al., Calibration of the dolomite clumped isotope thermometer from 25 to 350 °C: And implications for a universal calibration for all (Ca: Mg: Fe)CO₃ carbonates. *Geochim. Cosmochim. Acta* **200**, 255–279 (2017).

51. M. Daëron, D. Blamart, M. Peral, H. P. Affek, Absolute isotopic abundance ratios and the accuracy of Δ_{47} measurements. *Chem. Geol.* **441**, 83–96 (2016).

52. A. I. Fernandez et al., A reassessment of the precision of carbonate clumped isotope measurements: Implications for calibrations and paleoclimate reconstructions. *Geochem. Geophys. Geosyst.* **18**, 4375–4386 (2017).

53. W. A. Brand, S. S. Assonov, T. B. Coplen, Correction for the ^{17}O interference in $\delta^{13}C$ measurements when analyzing CO_2 with stable isotope mass spectrometry (IUPAC Technical Report). *Pure Appl. Chem.* **82**, 1719–1733 (2010).

54. S. M. Bernasconi et al., Reducing uncertainties in carbonate clumped isotope analysis through consistent carbonate-based standardization. *Geochem. Geophys. Geosyst.* **19**, 2895–2914 (2018).

55. W. F. Defliese, M. T. Hren, K. C. Lohmann, Compositional and temperature effects of phosphoric acid fractionation on Δ_{47} analysis and implications for discrepant calibrations. *Chem. Geol.* **396**, 51–60 (2015).

56. S. T. Murray, M. M. Arienzo, P. K. Swart, Determining the Δ_{47} acid fractionation in dolomites. *Geochim. Cosmochim. Acta* **174**, 42–53 (2016).

57. W. Guo, J. L. Mosenfelder, W. A. Goddard, J. M. Eiler, Isotopic fractionations associated with phosphoric acid digestion of carbonate minerals: Insights from first-principles theoretical modeling and clumped isotope measurements. *Geochim. Cosmochim. Acta* **73**, 7203–7225 (2009).

58. B. Chang et al., Effects of different constants and standards on the reproducibility of carbonate clumped isotope (Δ_{47}) measurements: Insights from a long-term dataset. *Rapid Commun. Mass Spectrom.* **34**, e8678 (2020).

59. J. Tang, M. Dietzel, A. Fernandez, A. K. Tripati, B. E. Rosenheim, Evaluation of kinetic effects on clumped isotope fractionation (Δ_{47}) during inorganic calcite precipitation. *Geochim. Cosmochim. Acta* **134**, 120–136 (2014).

60. S. Zaarur, H. P. Affek, M. T. Brandon, A revised calibration of the clumped isotope thermometer. *Earth Planet. Sci. Lett.* **382**, 47–57 (2013).

61. S. V. Petersen et al., Effects of improved ^{17}O correction on interlaboratory agreement in clumped isotope calibrations, Estimates of mineral-specific offsets, and temperature dependence of acid digestion fractionation. *Geochem. Geophys. Geosyst.* **20**, 1–25 (2019).

62. I. A. Müller et al., Calibration of the oxygen and clumped isotope thermometers for (proto-)dolomite based on synthetic and natural carbonates. *Chem. Geol.* **525**, 1–17 (2019).

63. S. M. McLennan, S. R. Hemming, S. R. Taylor, K. A. Eriksson, Rare earth elements in sedimentary rocks: Influence of provenance and sedimentary processes. *Rev. Mineral.* **21**, 169–200 (1989).

64. H. Jacob, Classification, structure, genesis and practical importance of natural solid oil bitumen ("migrabitumen"). *Int. J. Coal Geol.* **11**, 65–79 (1989).

65. C. E. Barker, M. Pawlewicz, "The correlation of vitrinite reflectance with maximum temperature in humic organic matter" in *Paleogeothermics*, G. Buntebarth, L. Stegena, Eds. (Lecture Notes in Earth Sciences, Springer, 1986), Vol. 5, pp. 79–93.

66. J. D. Pasteris, B. Wopenka, Raman spectra of graphite as indicators of degree of metamorphism. *Can. Mineral.* **29**, 1–9 (1991).

67. Y. Kouketsu et al., A new approach to develop the Raman carbonaceous material geothermometer for low-grade metamorphism using peak width. *Isl. Arc* **23**, 33–50 (2014).